A Multivariable Controller in Synchronous Frame Integrating Phase-Locked Loop to Enhance Performance of Three-Phase Grid-Connected Inverters in Weak Grids

Sushil Silwal, *Member, IEEE*, Masoud Karimi-Ghartemani, *Senior Member, IEEE*, Houshang Karimi, *Senior Member, IEEE*, Masoud Davari, *Senior Member, IEEE*, and Milad Hoseini Zadeh

Abstract—This paper presents a new current controller in the synchronous reference frame and its associated design for enhancing the performance of three-phase grid-connected inverters, especially against weak-grid conditions. The existing controllers do not perform strongly during high-impedance grid conditions and lead to oscillations and instability issues due to the interactions between the synchronization and control units. The proposed controller addresses this issue by 1) deriving a linear model of the three-phase phase-locked loop (PLL), 2) integrating the PLL model into the current controller design, 3) using a multivariable control design for multi-input multioutput systems, and 4) designing the controller gains using optimal linear quadratic theory. The proposed controller has superior performance over a substantially wider range of weakgrid conditions compared to conventional controllers. Extensive simulation and experimental results are presented in order to validate and reveal the desirable performance of the proposed controller.

Index Terms—Linear quadratic regulator (LQR), multi-input multi-output (MIMO) controller, phase-locked loop (PLL), three-phase grid-connected voltage-source converter (VSC), weak grids.

I. INTRODUCTION

Integrating distributed and renewable energy resources into the power grid is growing. Power electronic converters (PECs) interface the distributed energy resource (DER) devices while complying with the grid codes and standards [1]–[3]. PECs must robustly perform against system changes and uncertainties—such as a high-impedance grid (commonly known as the weak-grid condition)—where the frequency and voltage at the point of common coupling (PCC) can experience fluctuations. The converter dynamics amplify such conditions, so oscillations and instabilities occur [4]–[10]. The weak-grid

This work was supported by the U.S. National Science Foundation (NSF) grants under ECCS-EPCN Awards #1902791 and #1902787.

Sushil Silwal is with New York Independent System Operator, NY, USA, E-mail: ssilwal@nyiso.com.

Masoud Karimi-Ghartemani is with the Department of Electrical and Computer Engineering, Mississippi State University, Mississippi State, MS 39762, USA, E-mail: karimi@ece.msstate.edu.

Houshang Karimi and Milad Hoseini Zadeh are with the Department of Electrical Engineering, Polytechnique Montréal, Montréal, Québec H3T 1J4, Canada, E-mail: houshang.karimi@polymtl.ca, seyed-milad.hosseinizadeh@polymtl.ca.

Masoud Davari is with the Department of Electrical and Computer Engineering, Georgia Southern University, Statesboro, GA 30460, USA, E-mail: mdavari@georgiasouthern.edu; davari@ualberta.ca.

conditions limit the amount of power that an inverter can feed to the grid [7], [11]–[13]. A robust and optimal controller can increase the power transfer capacity of the inverter by allowing its operation closer to its steady-state stability limit, which is the maximum real power that the PECs can inject into the grid when the power is gradually increased.

In the control system of a grid-connected inverter, the phase-locked loop (PLL) [8], [14]–[17] is employed to extract the phase angle of grid voltage for synchronization, i.e., for the transformations between the *abc*- and *dq*-frames. The impacts of the PLL on weak-grid conditions have been extensively reported in many studies—e.g., see [8], [10], [12], [18]–[25]—they have revealed that the system stability margins are strongly affected by the PLL bandwidth.

Different approaches to enhancing the robustness of the inverter responses in weak-grid conditions by mitigating the adverse effects of PLL dynamics have been reported in the literature. The work in [4] shows that the stability of the overall converter depends on the real part of the admittance transfer function. This study recommends the bandwidth of PLL below one-tenth of that of the overall closed-loop control system such that the input conductance remains positive for most sub-synchronous frequencies. The decreased bandwidth, however, degrades the transient responses of the system. In [8], an input multiplicative perturbed model and a μ -synthesis approach to optimally synthesizing a robust ac-bus voltage controller have been proposed in order to enhance the whole system's robustness. Still, its design stage is complex and leads to synthesized controller transfer functions of a high order.

Studies in [26], [27] introduce a voltage feed-forward method to reduce the PLL instability effect during high-impedance grid conditions where the *q*-axis grid voltage is filtered and used in the *q*-channel of the current controller. The analysis and system performance for very weak-grid conditions are not presented. The work in [28] has introduced a similar current feed-forward method to improve the stability of the system. The work in [29] modifies the PLL via an impedance-based compensation term, allowing the inverter to synchronize to a virtual but stronger grid node. The design of the virtual impedance and the filters in the PLL constitute the challenges associated with this method. Along the same line, [11] has proposed considering an artificial stronger bus to operate the PLL on it. A power control method is introduced

in [30] where the capacitor voltage of the LCL filter is also controlled in the internal loop. This method causes the loss of current limiting, and the design of internal loop compensators to yield a robust operation can be challenging.

The work in [31] proposes damping of the post-fault oscillations amplified during weak-grid conditions, in droop-based grid-forming inverters, by using an adaptive virtual resistor. The study in [32] introduces a current-error-based angle and magnitude compensation strategy based on the classical voltage-source converter (VSC) vector control, which improves system stability and power transfer capability of the VSC connected to a very weak grid. The magnitude compensation is applied to the quadrature component of the reference voltage, and the angle compensation is added to the measured phase angle of the grid voltage. The study in [33] uses an impedance-compensated PLL where a filtered component of the output current is also employed to compensate for the output voltage. It, however, needs to switch between different controller designs for different grid strengths.

The studies in [34]–[37] have explored nonlinear control strategies. The study in [34] proposes an adaptive stabilizing control strategy within the PLL to damp the quadrature component of the grid voltage in order to minimize the oscillations due to loop interactions under low short-circuit ratio [SCR or equivalently short-circuit capacity ratio (SCCR) in [8]] and reduced grid voltage. The work presented in [35] accomplishes a combination of the PLL dynamics with the grid-connected VSI control using a disturbance observer integrated into the sliding mode control to address the uncertainties and external disturbance during weak-grid conditions. Similarly, [36] has used the feedback linearization method to develop a robust controller to regulate the active power and output voltage of the grid-connected VSC. This approach is shown to have a broader range of operations compared with the common vector control approach. The work in [36] investigates the stability and domain of attraction of the equilibrium point of the system; it uses the Lyapunov theorem to extend the domain of attraction of the equilibrium point. Such controllers are generally complex in design and analysis, and their performances within various operating conditions need to be studied.

To summarize, the existing approaches have improved the robustness of the inverter controller by either improving the feed-forward terms (coming from the PLL to the controller), synchronizing to a virtual but stronger grid node, adding more internal control loops, or exploring nonlinear control strategies. To the best of the authors' knowledge, none of them have been found to "integrate" the PLL into the three-phase current controller entirely via a multivariable controller and regard the PLL-integrated control synthesis as a multi-input multioutput (MIMO) design simultaneously. Although some have incorporated an "approximate" model of the PLL, e.g., a SISO transfer function model of the PLL, or looked at the PLL dynamics [34], [35], [38]–[40], they have not considered a MIMO system, a multivariable controller, and an exact PLL model concurrently. On the contrary, the method proposed in this paper accurately and thoroughly integrates a precise dynamic model of the PLL and current control methodologies thereby stabilizing all dynamics via one unified control ap-

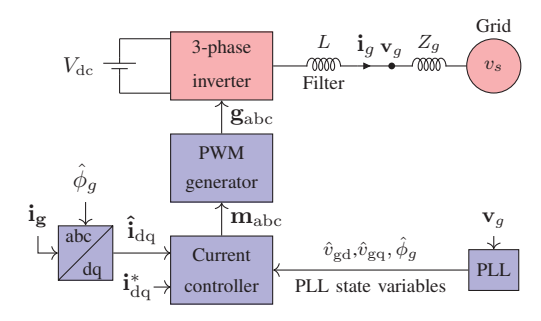


Fig. 1. System and controller of a grid-connected inverter.

proach. As a result, the proposed method is able to employ the accurate interconnected, detailed dynamics of three-phase grid-connected inverters to design a MIMO controller, which mathematically matches the problem under consideration. The work [41] has presented an approach to fully integrating the PLL in a single-phase inverter controller in the stationary frame using a large-signal linear time-invariant (LTI) model of the single-phase enhanced PLL (ePLL). It has demonstrated substantial performance enhancement in weak-grid conditions.

The approach based on the synchronous reference frame (SRF) (also known as the *dq*-frame control) together with SRF-PLL is widely applied to three-phase grid-connected converters in the power industry. This matter is studied in this paper. However, integrating PLL into the entire control design process and controller structure generally mitigates interactions between PLL and the control loop. Yet, the details associated with different PLLs and controllers should be investigated for each case. Recently, the same concept has been developed and applied to the controller in the stationary domain; see [42].

Compared with a single-phase system and the approach presented in [41], two significant differences need to be considered and addressed. 1) The dq-frame or SRF-PLL is employed, and the controller operates in the dq-frame, i.e., the rotating frame (not the stationary frame), and 2) the controller has two channels. In order to fully address the problem, it requires this paper to 1) derive a comprehensive LTI state-space model of the SRF-PLL suitable for control design integration and 2) develop a MIMO controller approach to avoiding the negative impact of decoupling terms [43] and establishing constructive coupling terms. This paper addresses these two aspects: 1) derivation of a PLL model and 2) formation and optimal design of a MIMO controller—including the PLL model. Extensive, comparative simulations and experimental results confirm and demonstrate the substantial improvement of the inverter performance in weak-grid conditions.

II. STUDY SYSTEM

The study system is a three-phase grid-connected VSC with the vector current controller implemented in the dq-frame. Figure 1 shows its complete block diagram. A stiff dc voltage (denoted by $V_{\rm dc}$) is assumed in this study. The VSC is connected to the grid at PCC via an L-filter whose inductance is properly chosen such that the peak-to-peak current ripple is sufficiently small, e.g., below 10% of the

TABLE I BASIC SYSTEM PARAMETERS

Parameter	Symbol	Value
Inverter power rating	S_{inv}	10 kVA
<i>L</i> -filter inductance (per phase)	L	4 mH
L-filter resistance (per phase)	R	1 mΩ
DC-bus voltage	$V_{ m dc}$	600 V
Grid voltage (L-N rms value)	V_s	120 V
Grid frequency	f_n	60 Hz
Grid inductance (per phase)	L_g	0–11 mH
Grid resistance (per phase)	R_g	$0.3\omega_n L_g \Omega$
Short-circuit ratio or	SCR or	1.000-10.976
short-circuit capacity ratio [8]	SCCR	(for L_g 10.976–1 mH)
Switching frequency	$f_{ m sw}$	10 kHz

peak rated current. A local load is connected to PCC. All the impedances reflecting the actual practical effects, such as the local grid impedance, the transformer impedance, and the line impedance, are considered and aggregated as grid impedance (denoted by Z_q). A weak grid is modeled through a Thévenin voltage source (v_s) behind the grid impedance Z_q , and the grid is weaker for larger amplitudes of practical Z_q s, i.e., $|Z_q|$, or equivalently lower SCRs/SCCRs (see [8] for their values for different grids). This approach to modeling a weak grid has been widely adopted in the research literature on weak-gridrelated studies [26]–[40]. Table I provides the set of parameters for the study system employed in the majority of simulations in this paper. For a fair comparison, both controllers are designed with the same criteria to achieve smoothness of transients with suitable damping and speed of response and without steadystate error over the widest possible range of grid strengths.

III. MIMO CONTROLLER

A MIMO controller based on an extended linear quadratic tracking approach has been recently proposed in [44] and has shown a superior performance. This method is regarded as the conventional controller here, forming a basis for developing the proposed controller design method. Therefore, this MIMO approach is briefly reviewed here.

The converter/grid current and voltage equations in the dq-frame are summarized as

$$L\frac{di_d}{dt} + Ri_d - \omega_g Li_q = u_d - v_{gd}$$

$$L\frac{di_q}{dt} + Ri_q + \omega_g Li_d = u_q - v_{gq}$$
(1)

where $v_{\rm gd}$, $v_{\rm gq}$ and i_d , i_q are the dq components of voltage ${\bf v_g}$ and current ${\bf i_g}$, respectively. Also, u_d and u_q are control inputs in the dq-frame. The transformation to/from dq uses $\hat{\phi}_g$ (from the PLL) as the reference angle. Moreover, ω_n is the nominal angular frequency and ω_q is the measured value.

For a common controller with PI (proportional-integral) terms, define the set of state variables as

$$x_1 = \int e_d dt$$
, $x_2 = \int e_q dt$, $x_3 = i_d$, $x_4 = i_q$

where $e_d = i_d^* - i_d$ and $e_q = i_q^* - i_q$ are the current tracking errors. The state equations will be

$$\dot{x}_1 = i_d^* - x_3, \quad \dot{x}_2 = i_q^* - x_4,
\dot{x}_3 = -\frac{R}{L}x_3 + \omega_g x_4 + \frac{1}{L}u_d + \frac{1}{L}v_{\text{gd}},
\dot{x}_4 = -\frac{R}{L}x_4 - \omega_g x_3 + \frac{1}{L}u_q + \frac{1}{L}v_{\text{gq}},$$
(2)

and the control vector is $\mathbf{u} = [u_d \ u_q]^T$.

The state equations and control inputs are linearly transformed by applying $\frac{d}{dt}$ to convert tracking problem into regulation problem. With $z=\frac{dx}{dt}$ and $w=\frac{du}{dt}$, the state equations and control law are re-written as

$$\dot{z}_{1} = -z_{3}, \quad \dot{z}_{2} = -z_{4},
\dot{z}_{3} = -\frac{R}{L}z_{3} + \omega_{g}z_{4} + \frac{1}{L}w_{d},
\dot{z}_{4} = -\frac{R}{L}z_{4} - \omega_{g}z_{3} + \frac{1}{L}w_{q}.$$
(3)

Equation (3) can be represented in state-space representation as $\dot{z} = Az + Bw$ where the matrices A and B are given by

$$A = \begin{bmatrix} 0 & 0 & -1 & 0 \\ 0 & 0 & 0 & -1 \\ 0 & 0 & -\frac{R}{L} & \omega_g \\ 0 & 0 & -\omega_g & -\frac{R}{L} \end{bmatrix}; B = \begin{bmatrix} 0 & 0 \\ 0 & 0 \\ \frac{1}{L} & 0 \\ 0 & \frac{1}{L} \end{bmatrix}.$$

As $x_1 = \int e_d dt$, it is obvious that $z_1 = e_d$, and similarly, $z_2 = e_q$. Moreover, $z_3 = \frac{d}{dt}i_d$, and $z_4 = \frac{d}{dt}i_q$. Thus, the controller gains are optimally designed to minimize the cost function $J = \int_0^\infty (z^T Q z + w^T R w) dt$, where Q is a positive semi-definite matrix with diagonal entries q_i , i = 1, ..., 4, and R is selected to be equal to the 2×2 identity matrix. Matrix Q is chosen according to the following steps.

Step I: Initialize q_1 and q_2 to small positive number around zero. Keep all other $q_i's$ at zero.

Step II: Start with q_1 and gradually increase it (followed by the same increase in q_2) such that the tracking error builds up to a desirable speed.

Step II: Increase q_3 and q_4 gradually such that all closed-loop poles have desired speed and damping.

By selecting the suitable values of diagonal elements $q_i's$ in \mathbf{Q} , the closed-loop poles are placed at the desired location, and the corresponding controller gain \mathbf{K} is found through $\mathbf{K} = lqr(\mathbf{A}, \mathbf{B}, \mathbf{Q}, \mathbf{R})$ —where "lqr" is a MATLAB command. Figure 2 shows the loci of all closed-loop poles with respect to an increase in q_i . First, q_1 is increased from 10^{-1} to $10^{5.5}$ followed by same increase in q_2 in order to penalize the tracking error in both d and q loops. Then, q_4 is gradually increased from 0 to 2 so as to achieve desired damping and speed of the system poles. The closed-loop poles are finally placed at $\begin{bmatrix} -304 \pm j468, -235 \pm j91 \end{bmatrix}$ with the controller gain $\mathbf{K} = \begin{bmatrix} -460.85 & 322.25 & 2.00 & -0.11 \\ -322.25 & -460.85 & -0.11 & 2.31 \end{bmatrix}$.

IV. PROPOSED CURRENT CONTROLLER

The common SRF-PLL that provides the synchronization angle for transformations to/from the dq-frame is shown in

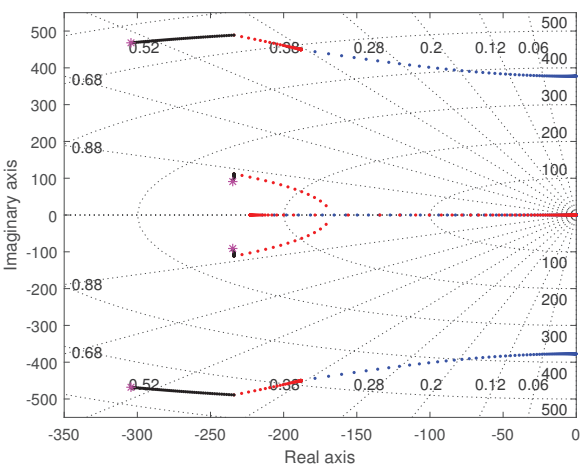


Fig. 2. Loci of closed-loop poles for $q_1 = [10^{-1} \to 10^{5.5}]$ (blue), $q_2 = [10^{-1} \to 10^{5.5}]$ (red), and $q_4 = [0 \to 2]$ (black).

Fig. 3. It is a nonlinear system of order three which can be characterized by three state variables. As it has been established in the literature that the dominant cause of system instability and oscillations during weak-grid conditions is the loop interactions between the PLL and the current controller, the central idea of the proposed controller is to integrate and incorporate these three state variables of the PLL into the MIMO controller. Fig. 4 shows the block diagram of the proposed multivariable controller. The state variables of the PLL are also incorporated in the controller design to address the instability issues caused by the weak-grid conditions.

Considering the effect of grid impedance and the PLL, the converter and grid voltage/current equations are written as

$$(L+L_g)\frac{d\hat{i}_d}{dt} + (R+R_g)\hat{i}_d - \omega_g(L+L_g)\hat{i}_q = \hat{v}_{gd} + \hat{u}_d - \hat{v}_{sd}$$

$$(L+L_g)\frac{d\hat{i}_q}{dt} + (R+R_g)\hat{i}_q + \omega_g(L+L_g)\hat{i}_d = \hat{v}_{gq} + \hat{u}_q - \hat{v}_{sq}$$
(4)

where $\hat{v}_{\rm sd}$, $\hat{v}_{\rm sq}$ are the dq components of $\mathbf{v_s}$. All the transformations are done using the PLL angle $\hat{\phi}_g$, where $\hat{\cdot}$ is used to denote the transformed variables.

For an integrating controller, define the state variables as

$$x_1 = \int e_d dt$$
, $x_2 = \int e_q dt$, $x_3 = \hat{i}_d$, $x_4 = \hat{i}_q$

where $e_d=i_d^*-\hat{i}_d$ and $e_q=i_d^*-\hat{i}_q$. Denoting $T_0=(L+L_g)^{-1},\ T_1=T_0(LR_g-L_gR),\ T_2=T_0L_g,\ {\rm and}\ T_3=T_0L,$ the state equations of the system and the controller are

$$\begin{split} \dot{x}_1 &= i_d^* - x_3, \quad \dot{x}_2 = i_q^* - x_4, \\ \dot{x}_3 &= T_0 \big[-(R + R_g) x_3 + \hat{v}_{\rm gd} + \hat{u}_d - \hat{v}_{\rm sd} \big] + \hat{\omega}_g x_4, \\ \dot{x}_4 &= T_0 \big[-(R + R_g) x_4 + \hat{v}_{\rm gg} + \hat{u}_g - \hat{v}_{\rm sg} \big] - \hat{\omega}_g x_3. \end{split} \tag{5}$$

A. PLL Model

Let x_5 , x_6 , and x_7 be the state variables of the PLL as defined and shown in Fig. 3. Considering $\mu = \mu_1 = \mu_3$

$$\dot{x}_5 = -\mu x_5 + \mu \hat{v}_{gd}, \ \dot{x}_6 = x_7 + \mu \frac{\hat{v}_{gq}}{x_5}, \ \dot{x}_7 = \mu_2 \frac{\hat{v}_{gq}}{x_5}.$$
 (6)

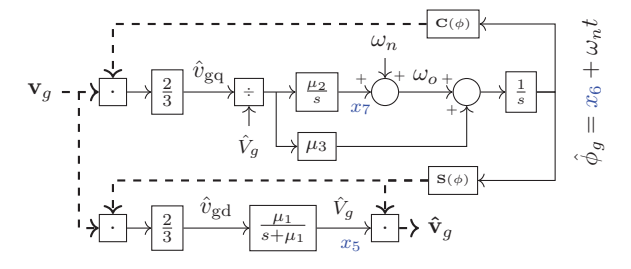


Fig. 3. Block diagram of the PLL [45].

Define the vectors S and C as

$$\mathbf{S}(\theta) = \begin{bmatrix} \sin(\theta) \\ \sin(\theta - 120) \\ \sin(\theta + 120) \end{bmatrix}, \ \mathbf{C}(\theta) = \begin{bmatrix} \cos(\theta) \\ \cos(\theta - 120) \\ \cos(\theta + 120) \end{bmatrix}.$$

Let $\mathbf{v_g}$ be voltage at PCC with peak value of V_g , $\mathbf{i_g}$ be the inverter output current with peak value I_g , and $\mathbf{v_s}$ be the stiff grid voltage with peak value of V_s . Thus, $\mathbf{v_s} = V_s \mathbf{S}(\phi_s)$, $\mathbf{v_g} = V_g \mathbf{S}(\phi_g)$, $\mathbf{i_g} = I_g \mathbf{S}(\phi_i)$. Subsequently,

$$\hat{v}_{sd} = \frac{2}{3} \mathbf{S}^{\mathbf{T}} (\hat{\phi}_{\mathbf{g}}) \mathbf{v}_{\mathbf{s}} = V_s \cos(\hat{\phi}_g - \phi_s) = V_s \cos(x_6)$$

$$\hat{v}_{sq} = \frac{2}{3} \mathbf{C}^{\mathbf{T}} (\hat{\phi}_{\mathbf{g}}) \mathbf{v}_{\mathbf{s}} = -V_s \sin(\hat{\phi}_g - \phi_s) = -V_s \sin(x_6)$$

Next, expressions for $\hat{v}_{\rm gd}$ and $\hat{v}_{\rm gq}$ are derived in terms of $\hat{v}_{\rm sd}$, $\hat{v}_{\rm sq}$ and other state variables. Applying KVL between $\mathbf{v_g}$ and $\mathbf{v_s}$ on the d axis yields

$$L_g \frac{d\hat{i}_d}{dt} + R_g \hat{i}_d - \hat{\omega}_g L_g \hat{i}_q = \hat{v}_{gd} - \hat{v}_{sd}. \tag{7}$$

By substituting (7) in (4) $\frac{d\hat{\imath}_d}{dt} = -\frac{R}{L}\hat{\imath}_d + \hat{\omega}_g\hat{\imath}_q + \frac{\hat{\imath}_d}{L} - \frac{\hat{v}_{\rm gd}}{L}$, L_g or L, one gets $\hat{v}_{\rm gd} = T_1x_3 + T_2\hat{u}_d + T_3V_s\cos(x_6)$. Similarly, $\hat{v}_{\rm gq} = T_1x_4 + T_2\hat{u}_q - T_3V_s\sin(x_6)$. Substituting $\hat{v}_{\rm gd}$ and $\hat{v}_{\rm gq}$ in (6), the PLL state equations can be derived as

$$\dot{x}_5 = -\mu x_5 + \mu [T_1 x_3 + T_2 \hat{u}_d + T_3 V_s \cos(x_6)]
\dot{x}_6 = x_7 + \frac{\mu}{x_5} [T_1 x_4 + T_2 \hat{u}_q - T_3 V_s \sin(x_6)]
\dot{x}_7 = \frac{\mu_2}{x_5} [T_1 x_4 + T_2 \hat{u}_q - T_3 V_s \sin(x_6)].$$
(8)

Finally, the complete state equations, including the two state variables of the system, two variables of integrators in the controller, and three variables of the PLL, are obtained as

$$\begin{split} \dot{x}_1 &= i_d^* - x_3, \quad \dot{x}_2 = i_q^* - x_4, \\ \dot{x}_3 &= -T_0 (R + R_g) x_3 + T_0 [T_1 x_3 + T_2 \hat{u}_d + T_3 V_s \cos(x_6)] \\ &\quad + \omega_n x_4 + T_0 \hat{u}_d - T_0 V_s \cos(x_6), \\ \dot{x}_4 &= -T_0 (R + R_g) x_4 + T_0 [T_1 x_4 + T_2 \hat{u}_q - T_3 V_s \sin(x_6)] \\ &\quad - \omega_n x_3 + T_0 \hat{u}_q + T_0 V_s \sin(x_6), \\ \dot{x}_5 &= -\mu x_5 + \mu [T_1 x_3 + T_2 \hat{u}_d + T_3 V_s \cos(x_6)] \\ \dot{x}_6 &= x_7 + \frac{\mu}{x_5} [T_1 x_4 + T_2 \hat{u}_q - T_3 V_s \sin(x_6)] \\ \dot{x}_7 &= \frac{\mu_2}{x_5} [T_1 x_4 + T_2 \hat{u}_q - T_3 V_s \sin(x_6)]. \end{split}$$

It is evident that the PLL nonlinearity penetrates into the entire system and makes the overall system nonlinear.

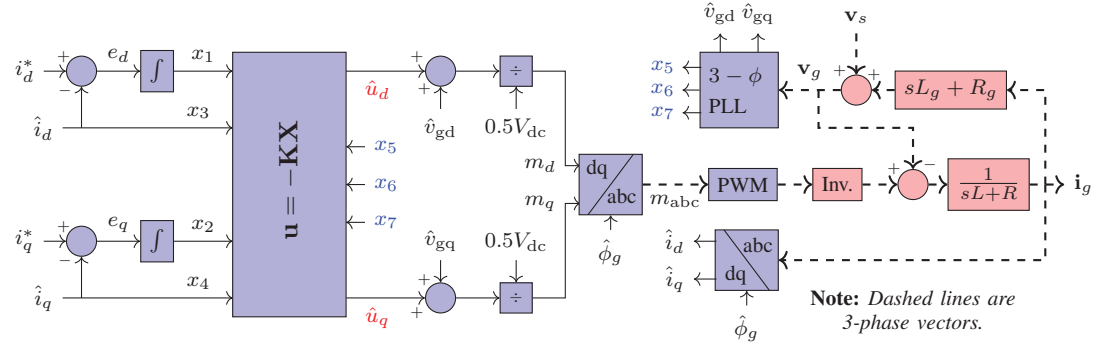


Fig. 4. Proposed multivariable, PLL-integrated current controller for three-phase grid-connected inverters.

B. Linearization of State Equations

The state equations (9) are linearized around the equilibrium point. In order to obtain the equilibrium point, first note that the currents at this point are $x_3^* = i_d^*$, $x_4^* = i_q^*$. For the nominal grid impedance of $(R_1 + j\omega_n L_1)$ and considering the phase of v_s as the reference, nominal amplitude (V_q^*) and phase angle (δ_a^*) of v_a^* can be found as

$$\mathbf{v}_{g}^{*} = (v_{\text{sd}} + jv_{\text{sq}}) + (i_{d}^{*} + ji_{q}^{*})(R_{1} + j\omega_{n}L_{1}),$$

$$= V_{s} + R_{1}i_{d}^{*} - \omega_{n}L_{1}i_{q}^{*} + j(R_{1}i_{q}^{*} + \omega_{n}L_{1}i_{d}^{*}),$$

$$\therefore V_{g}^{*} = \sqrt{(V_{s} + R_{1}i_{d}^{*} - \omega_{n}L_{1}i_{q}^{*})^{2} + (R_{1}i_{q}^{*} + \omega_{n}L_{1}i_{d}^{*})^{2}}, \quad (10)$$

$$\delta_{g}^{*} = \tan^{-1}\left[\frac{R_{1}i_{q}^{*} + \omega_{n}L_{1}i_{d}^{*}}{V_{s} + R_{1}i_{d}^{*} - \omega_{n}L_{1}i_{d}^{*}}\right].$$

Therefore, $x_5^* = V_g^*$, and $x_6^* = \delta_g^*$. During the steady-state, $\hat{u}_d^* - \hat{v}_{\mathrm{sd}}^* + \hat{v}_{\mathrm{gd}}^* = (R+R_1)i_d^*$ is valid, or equivalently,

$$(R+R_1)x_3^* = \hat{u}_d^* + T_1x_3^* + T_2\hat{u}_d^* + T_3V_s\cos x_6^* - V_s\cos x_6^*$$

$$\hat{u}_d^* = \frac{1}{1+T_2}[(R+R_1-T_1)x_3^* + (1-T_3)V_s\cos(x_6^*)]$$
(11)

Similarly, $\hat{u}_q^* = \frac{1}{1+T_2}[(R+R_1-T_1)x_4^* + (T_3-1)V_s\sin(x_6^*)].$ Then, the linearization around the equilibrium point is performed in order to derive

$$\dot{\tilde{\mathbf{x}}} = \mathbf{A}\tilde{\mathbf{x}} + \mathbf{B}\tilde{\mathbf{u}} \tag{12}$$

where $\tilde{\mathbf{x}} = \mathbf{x} - \mathbf{x}^* = [\tilde{x}_1 \ \tilde{x}_2 \ ... \ \tilde{x}_7]^T, \ \mathbf{x} = [x_1 \ x_2 \ ... \ x_7]^T, \ \mathbf{x}^* = [x_1^* \ x_2^* \ ... \ x_7^*]^T, \ \text{and} \ \mathbf{u} = [\hat{u}_d \ \hat{u}_q]^T. \ \text{The } a_{ij} \ \text{element of matrix } \mathbf{A} \ \text{and} \ b_{ij} \ \text{elements of matrix } \mathbf{B} \ \text{are calculated through}$

$$a_{ij} = \frac{\partial \dot{x}_i}{\partial x_j}\Big|_*, \ \forall \ i \in [1, .., 7], \ j \in [1, .., 7]$$

$$b_{ij} = \frac{\partial \dot{x}_i}{\partial u_j}\Big|_*, \ \forall \ i \in [1, .., 7], \ j \in [1, 2]$$
(13)

$$b_{ij} = \frac{\partial \dot{x}_i}{\partial u_i}\Big|_*, \ \forall \quad i \in [1, ..., 7], \quad j \in [1, 2]$$

as detailed in Appendix A.

C. Selection of PLL Gains

As shown in Fig. 3, the PLL has 3 gains—i.e., μ_1 , μ_2 , and μ_3 . With $\mu_1 = \mu_3 = \mu = 2\zeta_1\omega_n$ and $\mu_2 = \frac{\mu^2}{4\zeta_2^2}$, the characteristic equation of PLL is $s^2 + \mu s + \mu_2 = 0$. The damping ratio ζ_1 corresponds to the filtering level of the PLL. The damping ratio ζ_2 corresponds to the frequency estimation dynamics and inversely determines its bandwidth. In this study, $\zeta_1 = 0.4$, $\zeta_2 = 2$ are chosen which correspond to $\mu_1 = \mu_3 = 300$ and $\mu_2 = 5700$.

D. Optimal Design of Proposed Controller

In order to employ the linear quadratic regulator (LQR) approach to designing the controller gains, (12) is linearly transformed by applying $\frac{d}{dt}$ to its both sides to arrive at

$$\dot{\mathbf{z}} = \mathbf{A}\mathbf{z} + \mathbf{B}\mathbf{w} \tag{15}$$

where, $\mathbf{z} = \frac{d\mathbf{x}}{dt}$ and $\mathbf{w} = \frac{d\mathbf{u}}{dt}$. Then, the state variables z_1 and z_2 represent the tracking errors in the d and q axes, respectively. Therefore, the controller gains are optimally designed by minimizing the cost function $J = \int_0^\infty (z^T Q z + w^T R w) dt$, where Q is a positive semi-definite matrix with diagonal entries q_i , i = 1, 2, ..., 7, and R is the 2×2 identity matrix. The elements of matrix Q are selected through the following proposed steps.

Step I: Initialize q_1 and q_2 at a small positive number around zero. Keep all other $q_i's$ at zero.

Step II: Start with q_1 and gradually increase it followed by q_2 such that the tracking error builds up to a desirable speed. **Step III:** Increase q_4 gradually such that high frequency closed-loop complex poles have desired damping.

Step IV: Increase q_5 gradually to fine tune the speed and damping of all the closed-loop poles (including the PLL).

Figure 5 shows the loci of all closed-loop poles with respect to an increase in $q_i's$: q_1 from 10^{-1} to $10^{5.5}$ (blue), q_2 from 10^{-1} to 10^5 , q_4 from 0 to 6, and q_5 from 0 to 1. The closedloop poles are finally placed at $[-305 \pm j405, -158 \pm$ j10, -330, -91, -22] to have similar dynamics as conventional ones. The corresponding controller gain is K =-427.33205.552.11 -0.080.140.09-240.31-0.03-365.53-0.032.77 $49.71 \quad 0.07$

E. Robustness Analysis of Proposed Controller

The robustness of the proposed controller is compared with that of the conventional controllers against uncertainty in the grid inductance (L_q) using an eigenvalue analysis. Figure 6 shows that the poles of the conventional controller experience more significant location changes—and hence, shifting towards the imaginary axis—than location changes of the proposed controller's poles for both low and high power scenarios. This observation confirms the proposed controller's "higher" level of robustness against grid weakness.

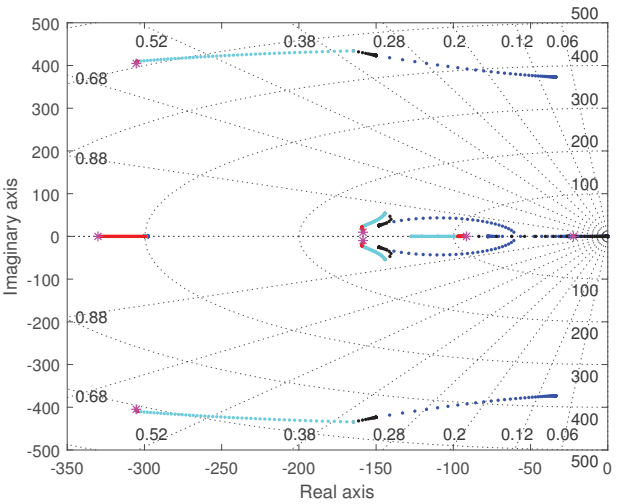


Fig. 5. Loci of close-loop poles of the proposed controller for $q_1 = [10^{-1} \rightarrow 10^{5.5}]$ (blue), $q_2 = [10^{-1} \rightarrow 10^{5}]$ (black), $q_4 = [0 \rightarrow 6]$ (cyan), and $q_5 = [0 \rightarrow 1]$ (red). The final locations are marked by asterisk (*).

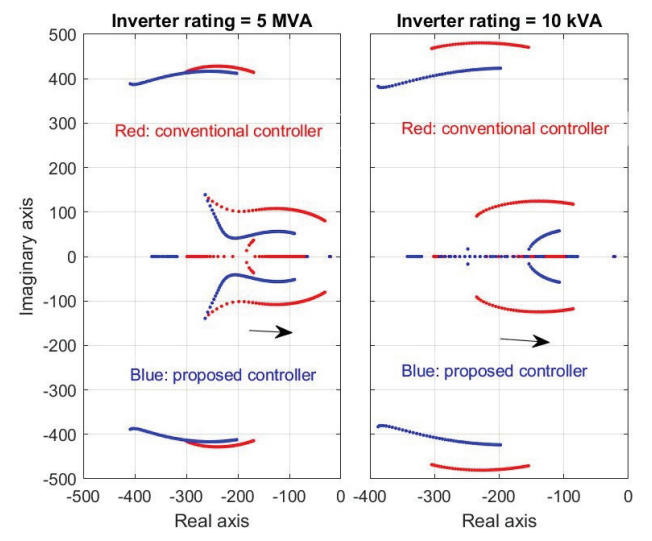


Fig. 6. Eigenvalues of the proposed and conventional controllers when L_g varies from 0 mH to 10 mH for high-power (left) and low-power (right) system.

V. SIMULATION RESULTS

Simulations are performed in the PSIM software for the selected system parameters and the designed controller gains. The operation and grid connection of the power inverter are sequentially performed. At first, the PLL is started, and the generated v_{gd} , v_{gq} by the PLL are used to have a soft start. The desired characteristics of the controllers are achieving fast and smooth transient response without any steady-state error for the widest possible range of grid strength or fault. Therefore, the stability margin of the conventional and proposed controllers at different grid strength levels are compared based on two conditions: 1) the power jump withstand capacity and 2) fault-ride-through capability. The power jump withstand capacity is defined as the maximum

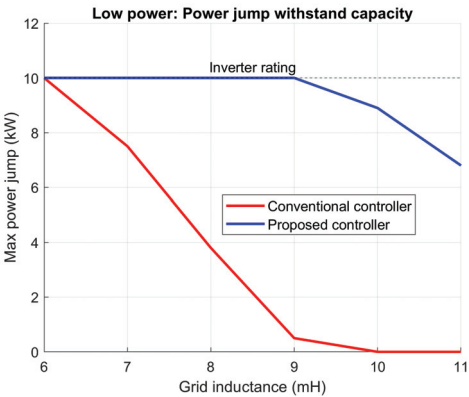


Fig. 7. Power jump withstand capacity of low-power inverter—in which SCR changes from 1.829 to 1.000 with respect to L_g variations from 6.000 mH to 10.976 mH, according to Table I.

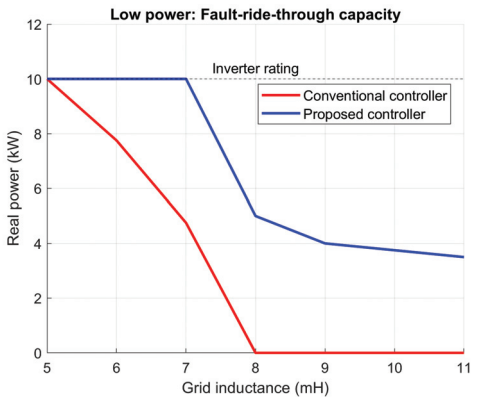


Fig. 8. Fault-ride-through capacity of low-power inverter—in which SCR changes from 2.195 to 1.000 with respect to L_g variations from 5 mH to 10.976 mH, according to Table I.

real power step command that the inverter system can execute without oscillatory transients leading to instability. These two conditions provide extreme case scenarios in which the inverter system can operate—depicting the robustness of the control system. These simulation results are collected and presented for a low-power inverter (10 kVA) and a high-power inverter (5 MVA).

A. Low-Power Inverter ($S_{inv} = 10 \text{ kVA}$)

The system parameters in Table I and the controller gains designed above are employed in this section. The grid inductance values of 1.000–10.976 mH correspond to the SCR values of 10.976–1.000, respectively.

- 1) Power Jump Withstand Capacity: Figure 7 shows the real power jump withstand capacity of both conventional and proposed controllers for different grid strength levels. Both controllers can withstand a rated power jump of 10 kW when L_g is less than 6 mH. As the grid inductance increases, the ability of the conventional controller to withstand power jump rapidly decreases and reaches close to zero for $L_g=9$ mH. However, the proposed controller can withstand rated power jump up until $L_g=9$ mH. It can withstand jump of 4 kW for $L_g=13$ mH. This shows a substantial level of improvement.
- 2) Fault Ride-Through Capacity: A three-phase fault with a voltage drop of 80% is applied at 1/4 distance from PCC in the

TABLE II HIGH-POWER SYSTEM AND CONTROL PARAMETERS

Parameter	Symbol	Value	
Inverter power rating	S_{inv}	5 MVA	
L-filter inductance (per phase)	L	2 mH	
DC-bus voltage	$V_{ m dc}$	8 kV	
Grid voltage (L-N rms value)	V_s	1.9 kV	
Grid inductance (per phase)	L_g	0–6 mH	
Short-circuit ratio or	SCR or	1.000-5.746	
short-circuit capacity ratio [8]	SCCR	(for L_g 5.746–1.0mH)	
Conventional controller gains:			
$\begin{bmatrix} -138.7 & 111.3 & 0.8 \end{bmatrix}$	83 -0.0	[9]	
$\mathbf{K} = \begin{bmatrix} -138.7 & 111.3 & 0.5 \\ -111.3 & -138.7 & -0.5 \end{bmatrix}$.09 1.1		
Proposed controller gains:			
-235.1 118.9 1.1	1 -0.04	0.16 251.9 1.9	

0.04

1.5

-0.03

833.7

0.4

interconnecting line for 0.05 seconds to observe its impact on controller performances. Figure 8 shows the fault ride-through capacity of both conventional and proposed controllers for different grid strength levels. Both controllers can inject rated power to the grid and ride through the fault when L_g is less than 5 mH. As the grid inductance increases, the ability of the conventional controller to inject power to the grid rapidly decreases and reaches zero for $L_g=8$ mH. However, the proposed controller can ride through fault while operating at rated power up until $L_g=7$ mH. Even for extremely weak-grid conditions, the proposed controller can ride through fault while functioning at more than 30% of rated capacity.

B. High-Power Inverter ($S_{inv} = 5 \text{ MVA}$)

-132.2

A 5-MVA inverter is chosen and the system parameters are properly chosen, and the controller gains are designed following similar steps as is in the low-power inverter scenario described. The system and control parameters are presented in Table II. The grid inductance values of 1.000–5.746 mH correspond to the SCR values of 5.746–1.00, respectively.

- 1) Power Jump Withstand Capacity: Figure 9 shows the real power jump withstand capacity of both conventional and proposed controllers for different grid strength levels. Both controllers can withstand a rated power jump of 5 MW up to $L_g=4$ mH. As the grid inductance increases, the ability of both controllers to withstand power jump gradually decreases. However, the proposed controller is able to withstand around 1 MW more power jumps for all grid strength levels.
- 2) Fault Ride-Through Capacity: Similar to the low-power scenario, a three-phase fault with a voltage drop of 80% is applied at 1/4 distance from PCC in the interconnecting line for 0.05 seconds to observe its impact on controller performances. Figure 10 shows the fault ride-through capacity of both conventional and proposed controllers for different grid strength levels. It shows that the proposed controller has better fault tolerance for the entire range of grid impedance except when 5.5 mH< $L_{\rm g}$ < 6.25 mH where the conventional controller performs marginally better than the proposed one.

VI. EXPERIMENTAL RESULTS

A test bed/rig available in the lab (as described below) is employed to validate the performance and implementation of the proposed controller and shows its practicability. Figure 11

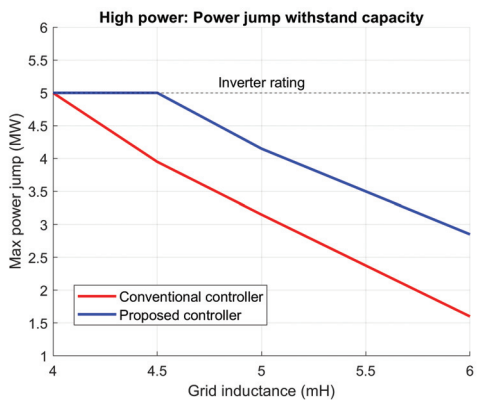


Fig. 9. Power jump withstand capacity of high-power inverter—in which SCR changes from 1.436 to 1.000 with respect to L_g variations from 4.000 mH to 5.746 mH, according to Table II.

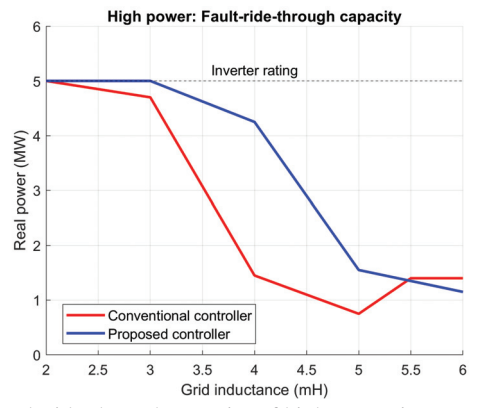


Fig. 10. Fault ride-through capacity of high-power inverter—in which SCR changes from 2.873 to 1.000 with respect to L_g variations from 2.000 mH to 5.746 mH, according to Table II.

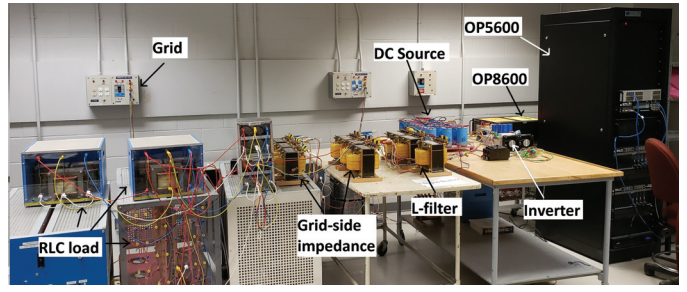


Fig. 11. Experimental set-up.

shows a photograph of the experimental test bed/rig used to test the proposed controller. The controllers are implemented in the real-time simulator OP5600 from OPAL-RT Technologies. The OP5600 generates the switching pulses for a 20 kVA Semikron SKH161 inverter which has six IGBTs with drivers. The dc source of 160 V is built using a 3-phase passive rectifier connected to an auto-transformer. The auto-transformer input is connected to a three-phase transformer which reduces the grid of 120 V (line-to-neutral rms value) to 30 V (line-to-neutral rms value). The inverter, designed for the base current of 10.2 A, is connected via an L-filter of 5 mH to the grid. A parallel RLC ($R=15~\Omega,~L=55~\text{mH},~C=38~\mu\text{F}$) load is connected at PCC, and an impedance is connected between the grid and PCC to mimic weak-grid conditions. The voltage

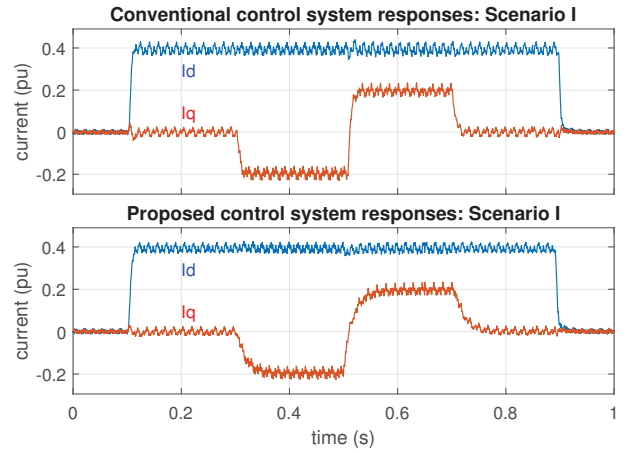


Fig. 12. Scenario I ($L_q = 0$ mH): inverter current in the dq-frame.

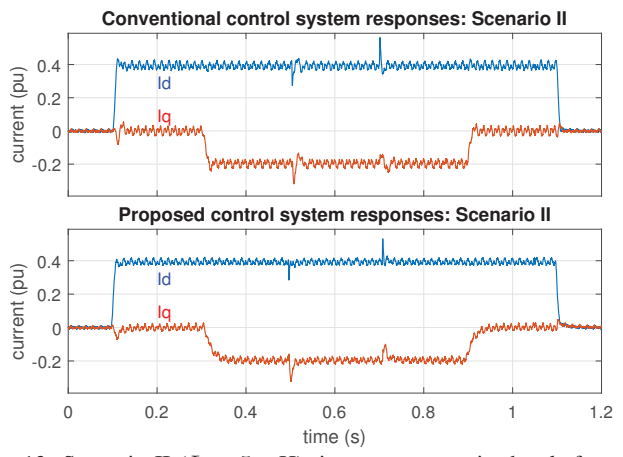


Fig. 13. Scenario II ($L_g = 5$ mH): inverter current in the dq-frame.

and current waveforms are measured by the OP8660 sensor and then forwarded to the OP5600. The data from OPAL-RT are saved and plotted using MATLAB. Multiple scenarios have been implemented and tested as described below.

Since it was not feasible to emulate grid faults in our experiments, the disturbance of the load connection/disconnection in weak grid conditions is considered. This produces a momentary voltage change which is somewhat similar to a voltage sag during grid faults even though not to the same extent. Therefore, a similar conclusion about the relative robustness of the proposed controller against grid faults can be anticipated.

Scenario I—Strong Grid—In this scenario, there is no impedance between PCC and the grid. The system is started with zero current. The following sequence of disturbances are applied: I_d increases from 0 to 4 A [0.4 per unit (pu)] at $t=0.1\,$ s, I_q decreases from 0 to -2 A (-0.2 pu) at $t=0.3\,$ s, I_q jump from -2 to 2 A (0.2 pu) at $t=0.5\,$ s, I_q goes back to 0 at $t=0.7\,$ s and finally I_d returns to 0 at $t=0.9\,$ s. Figure 12 shows the inverter current in the dq-frame. Both controllers perform well and similar in this scenario. The transient response of the I_q signal is acceptably damped with a time constant and a settling time in the order of one cycle and two cycles, respectively.

Scenario II—Mildly Weak Grid—In this scenario, there is an impedance of 5 mH inserted between PCC and the

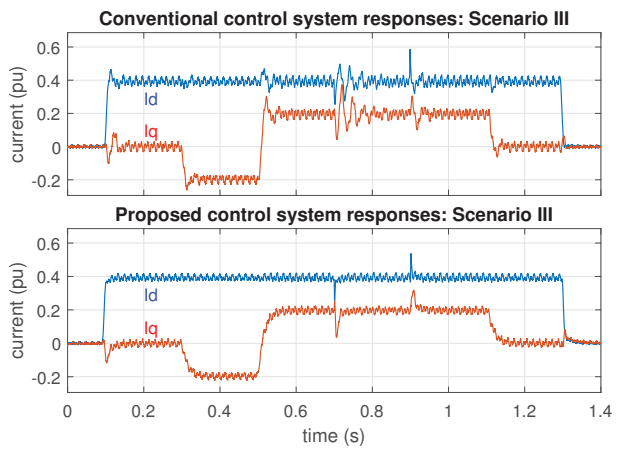


Fig. 14. Scenario III ($L_q = 10$ mH): inverter current in the dq-frame.

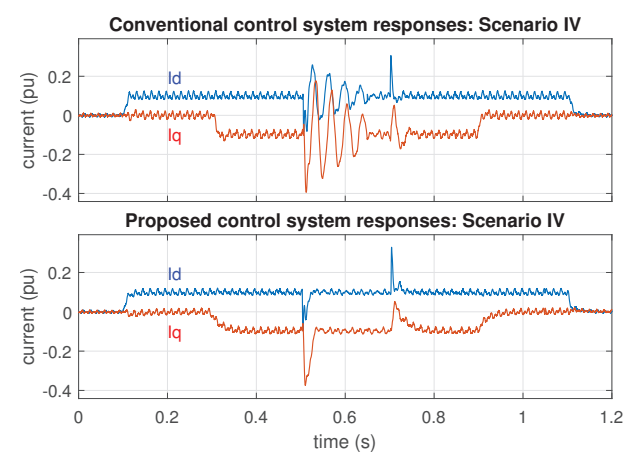


Fig. 15. Scenario IV ($L_g = 20$ mH): inverter current in the dq-frame.

grid. The system is started with zero current, and the RLC load is connected. The following sequence of disturbances are applied: I_d increases from 0 to 4 A (0.4 pu) at t=0.1 s, I_q decreases from 0 to -2 A (-0.2 pu) at t=0.3 s, local load is disconnected at t=0.5 s and reconnected at t=0.7 s, I_q goes back to 0 at t=0.9 s and finally I_d returns to 0 at t=1.1 s. Figure 13 shows the inverter current in the dq-frame. The performances of both controllers are similar—with the proposed controller being marginally better in terms of overshoots and settling time.

Scenario III—Weak Grid—In this scenario, an impedance of 10 mH is inserted between PCC and the grid. The system is started at zero current, and the RLC load is connected. The following sequence of disturbances are applied: I_d increases from 0 to 4 A (0.4 pu) at t=0.1 s, I_q decreases from 0 to -2 A (-0.2 pu) at t=0.3 s, I_q increases from -2 to 2 A (0.2 pu) at t=0.5 s, local load is disconnected at t=0.7 s and reconnected at t=0.9 s, I_q goes back to 0 at t=1.1 s and finally I_d returns to 0 at t=1.3 s. Figure 14 shows the inverter current in the dq-frame. The performance of the conventional control system is oscillatory and is approaching the instability region—especially when the local load is disconnected. However, the performance of the proposed controller has smooth transients without oscillations.

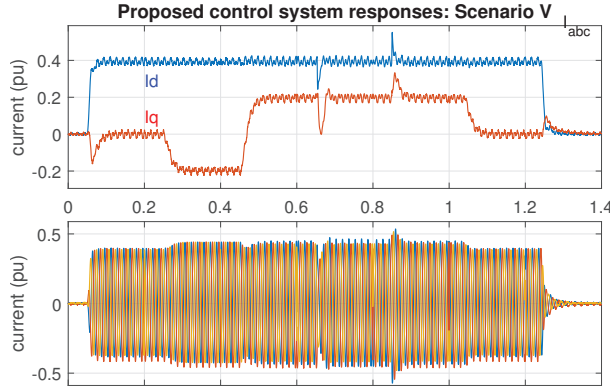


Fig. 16. Scenario V ($L_q = 20$ mH): (proposed) inverter current.

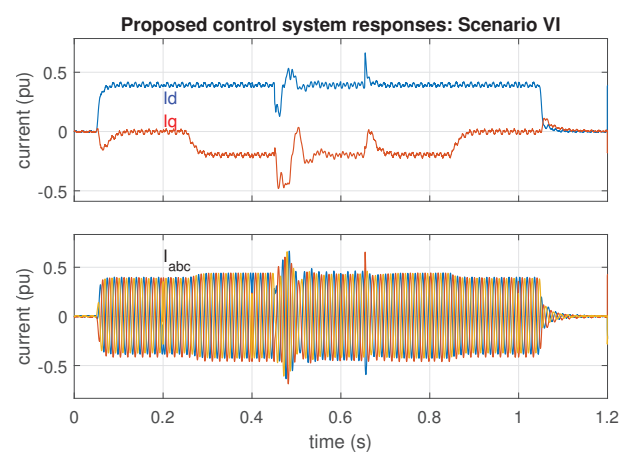


Fig. 17. Scenario VI ($L_q = 25$ mH): (proposed) inverter current.

Scenario IV—Very Weak Grid and Small Power Jumps—In this scenario, an impedance of 20 mH is connected between PCC and the grid. The system is started with zero current, and the RLC load is connected. A step change of 2 A in I_d is applied at $t\!=\!0.1$ s followed by a step change of -1 A (-0.1 pu) in I_q at $t\!=\!0.3$ s. The local load is disconnected at $t\!=\!0.5$ s and is reconnected at $t\!=\!0.7$ s. I_q returns to 0 at $t\!=\!0.9$ s and I_d goes back to zero at $t\!=\!1.1$ s. The inverter output currents in the dq-frame is shown in Fig. 15. The conventional control system's response is highly oscillatory and is on the brink of instability even for such a low-power operation. However, the proposed control system responds robustly to the applied disturbances with short and smooth transients.

Scenario V—Very Weak Grid and Large Power Jumps—Figure 16 shows that the proposed controller performs well with smooth transients even for large step changes in the current reference and the connection/disconnection of the load.

Scenario VI—*Extremely Weak Grid and Large Power Jumps*—In this scenario, the grid impedance is further increased to 25 mH. Figure 17 shows that the proposed system is still stable and performs satisfactorily.

Scenario VII—*Transients in ABC Current*—Figure 18 compares the transient response of both controllers for two grid strength levels when 2 A (0.2 pu) jump in real current I_d is applied. Due to the unavailability of a three-channel oscilloscope, only the currents of two phases with the vertical axis of 0.1 pu/div (for current) and the horizontal axis of 20

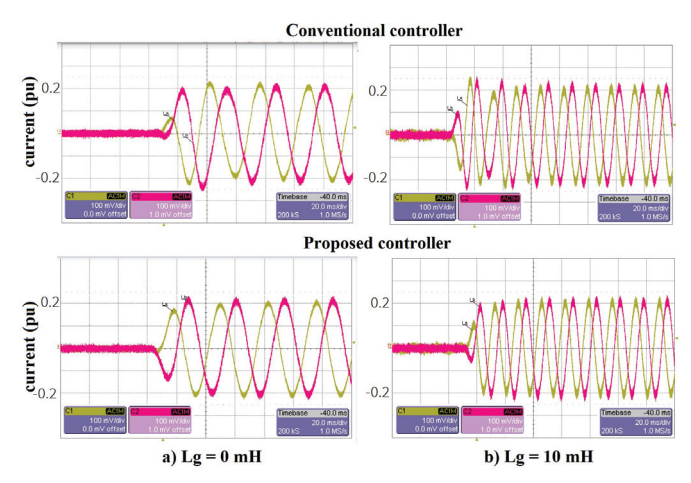


Fig. 18. Current jump transients for both controllers in strong and weak grid conditions shown on a two-channel oscilloscope (vertical axis is 0.1 pu/div for current, and horizontal axis is 20 ms/div).

ms/div are presented. The current of the third phase can be computed since the configuration is a three-wire system.

VII. CONCLUSION

This paper has proposed and studied a new controller for the three-phase grid-connected inverters that use vector current control in the synchronous rotating frame. The ideas of the paper have been summarized as 1) employing a multivariable controller (instead of two separate channels) and 2) including the dynamics of the phase-locked loop (PLL) in the controller. An appropriate linear time-invariant model of the three-phase PLL has been derived and incorporated within the multivariable current controller—whose entire control gains have been designed via an optimal control theory approach. An algorithm for the systematic design of the whole controller gains has also been proposed. Comparative simulations and experimental results have been included to confirm the robustness of the proposed controller for the entire range of strong to extremely weak-grid conditions.

APPENDIX A

CALCULATION OF MATRICES OF LINEARIZED MODEL

Elements of matrix **B** are calculated according to (14) as $b_{31}=T_0T_2+T_0; \quad b_{42}=T_0T_2+T_0, b_{51}=\mu T_2; \quad b_{62}=\frac{\mu}{x_5^*}T_2; \quad b_{72}=\frac{\mu_2}{x_5^*}T_2.$ All other elements are zero. Elements of matrix **A** are calculated according to equation (13) as

 $a_{13} = -1;$ $a_{24} = -1;$ $a_{33} = -T_0(R + R_q) + T_0T_1;$

$$\begin{aligned} a_{34} &= \omega_n; \quad a_{36} &= -T_0 T_3 V_s \sin(x_6^*) + T_0 V_s \sin(x_6^*); \\ a_{43} &= -\omega_n; \quad a_{44} &= -T_0 (R + R_g) + T_1 T_0; \\ a_{46} &= -T_0 T_3 V_s \cos(x_6^*) + T_0 V_s \cos(x_6^*); \\ a_{53} &= \mu T_1; \quad a_{55} &= -\mu; \quad a_{56} &= -\mu T_3 V_s \sin(x_6^*); \\ a_{64} &= \mu \frac{T_1}{x_5^*}; \quad a_{65} &= \frac{\mu}{x_5^{*2}} \{ T_1 x_4^* + T_2 \hat{u}_q^* - T_3 V_s \sin(x_6^*) \}; \\ a_{66} &= -\frac{\mu}{x_5^*} T_3 V_s \cos(x_6^*), \quad a_{67} &= 1, \quad a_{74} &= \mu_2 \frac{T_1}{x_5^*}, \\ a_{75} &= \frac{\mu_2}{x_5^{*2}} [T_1 x_4^* + T_2 \hat{u}_q^* - T_3 V_s \sin x_6^*]; a_{76} &= -\frac{\mu_2}{x_5^*} T_3 V_s \cos x_6^*. \end{aligned}$$

All other elements in ${\bf A}$ are equal to zero.

REFERENCES

- [1] "IEEE application guide for IEEE Std. 1547, IEEE standard for interconnecting distributed resources with electric power systems," *IEEE Std* 1547.2-2008, pp. 1–217, April 2009.
- [2] UL1741 Standard, "Standard for inverters, converters, controllers and interconnection system equipment for use with distributed energy resources," Jan 2010.
- [3] California Public Utility Commission, "Rule 21 interconnection," July 2017.
- [4] L. Harnefors, M. Bongiorno, and S. Lundberg, "Input-admittance calculation and shaping for controlled voltage-source converters," *IEEE Trans. Industrial Electronics*, vol. 54, no. 6, pp. 3323–3334, Dec. 2007.
- [5] W. Du, W. Dong, and H. F. Wang, "Small-signal stability limit of a grid-connected PMSG wind farm dominated by the dynamics of PLLs," *IEEE Trans. Power Systems*, vol. 35, no. 3, pp. 2093–2107, May 2019.
- [6] D. Yang, X. Ruan, and H. Wu, "Impedance shaping of the grid-connected inverter with LCL filter to improve its adaptability to the weak grid condition," *IEEE Transactions on Power Electronics*, vol. 29, no. 11, pp. 5795–5805, Nov. 2014.
- [7] Y. Huang, X. Yuan, J. Hu, P. Zhou, and D. Wang, "DC-bus voltage control stability affected by AC-bus voltage control in VSCs connected to weak AC grids," *IEEE Journal of Emerging and Selected Topics in Power Electronics*, vol. 4, no. 2, pp. 445–458, Jun. 2016.
- [8] M. Davari and Y. A.-R. I. Mohamed, "Robust vector control of a very weak-grid-connected voltage-source converter considering the phase-locked loop dynamics," *IEEE Transactions on Power Electronics*, vol. 32, no. 2, pp. 977–994, Feb. 2017.
- [9] N. P. Strachan and D. Jovcic, "Stability of a variable-speed permanent magnet wind generator with weak AC grids," *IEEE Transactions on Power Delivery*, vol. 25, no. 4, pp. 2779–2788, Oct. 2010.
- [10] D. Dong, B. Wen, D. Boroyevich, P. Mattavelli, and Y. Xue, "Analysis of phase-locked loop low-frequency stability in three-phase grid-connected power converters considering impedance interactions," *IEEE Transac*tions on Industrial Electronics, vol. 62, no. 1, pp. 310–321, Jan. 2015.
- [11] M. F. M. Arani and Y. A.-R. I. Mohamed, "Analysis and performance enhancement of vector-controlled VSC in HVDC links connected to very weak grids," *IEEE Transactions on Power Systems*, vol. 32, no. 1, pp. 684–693, Jan. 2017.
- [12] Y. Huang, X. Yuan, J. Hu, and P. Zhou, "Modeling of VSC connected to weak grid for stability analysis of DC-link voltage control," *IEEE Journal of Emerging and Selected Topics in Power Electronics*, vol. 3, no. 4, pp. 1193–1204, Dec. 2015.
- [13] R. Fu, L. Li, X. Wang, and X. Lv, "Critical SCR for the stability of VSC connected to weak grid," in *Proceeding of the 2020 IEEE Power & Energy Society General Meeting (PESGM)*. IEEE, 2020, pp. 1–5.
- [14] M. K. Ghartemani, S. A. Khajehoddin, P. K. Jain, and A. Bakhshai, "Problems of startup and phase jumps in PLL systems," *IEEE Transactions on Power Electronics*, vol. 27, no. 4, pp. 1830–1838, Apr. 2012.
- [15] F. Gonzalez-Espin, G. Garcerá, I. Patrao, and E. Figueres, "An adaptive control system for three-phase photovoltaic inverters working in a polluted and variable frequency electric grid," *IEEE Transactions on Power Electronics*, vol. 27, no. 10, pp. 4248–4261, Oct. 2012.
- [16] K.-J. Lee, J.-P. Lee, D. Shin, D.-W. Yoo, and H.-J. Kim, "A novel grid synchronization PLL method based on adaptive low-pass notch filter for grid-connected PCS," *IEEE Transactions on Industrial Electronics*, vol. 61, no. 1, pp. 292–301, Jan. 2014.
- [17] Z. Ali, N. Christofides, L. Hadjidemetriou, E. Kyriakides, Y. Yang, and F. Blaabjerg, "Three-phase phase-locked loop synchronization algorithms for grid-connected renewable energy systems: A review," *Renewable and Sustainable Energy Reviews*, vol. 90, pp. 434–452, Jul. 2018.
- [18] B. Wen, D. Boroyevich, R. Burgos, P. Mattavelli, and Z. Shen, "Analysis of D-Q small-signal impedance of grid-tied inverters," *IEEE Transactions on Power Electronics*, vol. 31, no. 1, pp. 675–687, Jan. 2015.
- [19] J. Z. Zhou, H. Ding, S. Fan, Y. Zhang, and A. M. Gole, "Impact of short-circuit ratio and phase-locked-loop parameters on the small-signal behavior of a VSC-HVDC converter," *IEEE Transactions on Power Delivery*, vol. 29, no. 5, pp. 2287–2296, Oct. 2014.
- [20] J. F. Morris, K. H. Ahmed, and A. Egea-Alvarez, "Analysis of controller bandwidth interactions for vector-controlled VSC connected to very weak AC grids," *IEEE Journal of Emerging and Selected Topics in Power Electronics*, pp. 1–1, 2020, Early Access. [Online]. Available: doi:10.1109/JESTPE.2020.3031203
- [21] L. Yang, Z. Chen, X. Zhou, W. Wu, W. Tan, J. Guerrero et al., "Effect of phase locked loop on small-signal perturbation modeling and stability

- analysis for three-phase LCL-type inverter connected to weak grid," *IET Renewable Power Generation*, Jun. 2018.
- [22] C. Zhang, X. Wang, and F. Blaabjerg, "Analysis of phase-locked loop influence on the stability of single-phase grid-connected inverter," in Proceedings of the 6th International Symposium on Power Electronics for Distributed Generation Systems (PEDG). IEEE, 2015, pp. 1–8.
- [23] T. Midtsund, J. Suul, and T. Undeland, "Evaluation of current controller performance and stability for voltage source converters connected to a weak grid," in *Proceedings of the 2nd International Symposium on Power Electronics for Distributed Generation Systems (PEDG)*. IEEE, 2010, pp. 382–388.
- [24] J. Xu, Q. Qian, B. Zhang, and S. Xie, "Harmonics and stability analysis of single-phase grid-connected inverters in distributed power generation systems considering phase-locked loop impact," *IEEE Transactions on Sustainable Energy*, vol. 10, no. 3, pp. 1470–1480, Jul. 2019.
- [25] G. Wu, H. Sun, X. Zhang, A. Egea-Alvarez, B. Zhao, S. Xu, S. Wang, and X. Zhou, "Parameter design oriented analysis of the current control stability of the weak-grid-tied VSC," *IEEE Transactions on Power Delivery*, vol. 36, no. 3, pp. 1458–1470, Jun. 2020.
- [26] X. Zhang, D. Xia, Z. Fu, G. Wang, and D. Xu, "An improved feedforward control method considering PLL dynamics to improve weak grid stability of grid-connected inverters," *IEEE Transactions on Industry Applications*, vol. 54, no. 5, pp. 5143–5151, Sep./Oct. 2018.
- [27] Z. Xie, Y. Chen, W. Wu, W. Gong, and J. M. Guerrero, "Stability enhancing voltage feed-forward inverter control method to reduce the effects of phase-locked loop and grid impedance," *IEEE Journal of Emerging and Selected Topics in Power Electronics*, vol. 9, no. 3, pp. 3000–3009, Jun. 2020.
- [28] J. Xu, S. Bian, Q. Qian, H. Qian, and S. Xie, "Robustness improvement of single-phase inverters under weak grid cases by adding grid current feedforward in delay-based phase-locked loop," *IEEE Access*, vol. 8, pp. 124 275–124 287, Jul. 2020.
- [29] J. A. Suul, S. D'Arco, P. Rodriguez, and M. Molinas, "Extended stability range of weak grids with voltage source converters through impedanceconditioned grid synchronization," in 11th IET International Conference on AC and DC Power Transmission, 2015, pp. 1–10.
- [30] S. Sang, N. Gao, X. Cai, and R. Li, "A novel power-voltage control strategy for the grid-tied inverter to raise the rated power injection level in a weak grid," *IEEE Journal of Emerging and Selected Topics in Power Electronics*, vol. 6, no. 1, pp. 219–232, Mar. 2017.
- [31] S. P. Me, S. Zabihi, F. Blaabjerg, and B. Bahrani, "Adaptive virtual resistance for post-fault oscillation damping with grid-forming control," *IEEE Transactions on Power Electronics*, pp. 1–1, 2021, Early Access. [Online]. Available: doi:10.1109/TPEL.2021.3118677
- [32] K. Givaki, D. Chen, and L. Xu, "Current error based compensations for vsc current control in weak grids for wind farm applications," *IEEE Transactions on Sustainable Energy*, vol. 10, no. 1, pp. 26–35, Jan. 2018.
- [33] S. Lu, Z. Xu, L. Xiao, W. Jiang, and X. Bie, "Evaluation and enhancement of control strategies for VSC stations under weak grid strengths," *IEEE Trans. Power Systems*, vol. 33, no. 2, pp. 1836–1847, Mar. 2017.
- [34] D. Pal and B. K. Panigrahi, "A nonlinear adaptive stabilizing control strategy to enhance dynamic stability of weak grid-tied VSC system," *IEEE Transactions on Power Delivery*, pp. 1–1, 2021, Early Access. [Online]. Available: doi:10.1109/TPWRD.2021.3106682
- [35] M. Davari, M. P. Aghababa, F. Blaabjerg, and M. Saif, "A modular adaptive robust nonlinear control for resilient integration of VSIs into emerging modernized microgrids," *IEEE Journal of Emerging and Selected Topics in Power Electronics*, vol. 9, no. 3, pp. 2907–2925, Jun. 2021.
- [36] M. Z. Mansour, S. Hadavi, and B. Bahrani, "Stability analysis and nonlinear control of phase locked loop of a weak-grid connected voltage source converter," in *Proceedings of the 2020 Fifteenth International* Conference on Ecological Vehicles and Renewable Energies (EVER). IEEE, 2020, pp. 1–6.
- [37] J. Khazaei, Z. Tu, A. Asrari, and W. Liu, "Feedback linearization control of converters with lcl filter for weak ac grid integration," *IEEE Transactions on Power Systems*, vol. 36, no. 4, pp. 3740–3750, Jul. 2021.
- [38] M. G. Taul, C. Wu, S.-F. Chou, and F. Blaabjerg, "Optimal controller design for transient stability enhancement of grid-following converters under weak-grid conditions," *IEEE Transactions on Power Electronics*, vol. 36, no. 9, pp. 10251–10264, Sep. 2021.
- [39] C. Li, S. Wang, F. Colas, and J. Liang, "Dominant instability mechanism of VSI connecting to a very weak grid," *IEEE Transactions* on *Power Systems*, pp. 1–1, 2021, Early Access. [Online]. Available: doi:10.1109/TPWRS.2021.3115968
- [40] R. Rosso, S. Engelken, and M. Liserre, "Robust stability investigation of the interactions among grid-forming and grid-following converters,"

- IEEE Journal of Emerging and Selected Topics in Power Electronics, vol. 8, no. 2, pp. 991–1003, Jun. 2020.
- [41] S. Silwal, S. Taghizadeh, M. Karimi-Ghartemani, M. J. Hossain, and M. Davari, "An enhanced control system for single-phase inverters interfaced with weak and distorted grids," *IEEE Transactions on Power Electronics*, vol. 34, no. 12, pp. 12538–12551, Dec. 2019.
- [42] S. M. Hoseinizadeh, H. Karimi, M. K. Ghartemani, and S. Ouni, "A multivariable pll-integrated controller for enhanced performance of voltage source converters under weak grid conditions," *IEEE Transactions on Industrial Electronics*, 2022.
- [43] S. Silwal, M. Karimi-Ghartemani, R. Sharma, and H. Karimi, "Impact of feed-forward and decoupling terms on stability of grid-connected inverters," in *Proceedings of the 2019 IEEE 28th International Symposium* on *Industrial Electronics (ISIE)*. IEEE, 2019, pp. 2641–2646.
- [44] M. Karimi-Ghartemani and H. Karimi, "A robust multivariable approach for current control of voltage-source converters in synchronous frame," *IEEE Journal of Emerging and Selected Topics in Power Electronics*, vol. 9, no. 5, pp. 6174–6183, Oct. 2020.
- [45] M. Karimi-Ghartemani, "Linear and pseudolinear enhanced phased-locked loop (EPLL) structures," *IEEE Transactions on Industrial Electronics*, vol. 61, no. 3, pp. 1464–1474, Mar. 2014.



Sushil Silwal (S'15–M'20) received his Ph.D. degree in Electrical and Computer Engineering (ECE) from Mississippi State University (MSU), Starkville, US, in 2019. Upon graduation, he worked in the same alma mater as a Postdoctoral Associate on innovative approaches for robust and reliable operation of voltage source converters in critical condition of emerging grids. He also worked as Postdoctoral Scholar in the Center for Energy Research at University of California San Diego on optimization and control of latest emerging grid technologies such as

battery energy storage systems, electrical vehicles, grid interactive microgrids, and smart plug loads. Currently he is working as Planning Engineer at New York Independent System Operator on reliability assessment of bulk power system. He has research and engineering interest in control, optimization, and reliability challenges of emerging power grid.



Masoud Karimi Ghartemani (SM'09) received his Ph.D. degree in Electrical and Computer Engineering from the University of Toronto, Canada, in 2004. Subsequently, he worked at Sharif University of Technology, Tehran, and Queen's University, Ontario, before joining the Department of Electrical and Computer Engineering at the Mississippi State University (MSU), USA, in 2012, where he is currently a Professor. His research interest includes modeling and control of distributed and renewable energy systems. Dr. Karimi is the recipient of 2020

Faculty Research Award in the Bagley College of Engineering at MSU. He is an Associate Editor for IEEE Transactions on Industrial Electronics, and IEEE Transactions on Sustainable Energy.



Houshang Karimi (SM'12) received his PhD degree in Electrical Engineering from University of Toronto, Toronto, ON, Canada, in 2007. From 2009 to 2012, he was an Assistant Professor with the Department of Electrical Engineering, Sharif University of Technology, Tehran, Iran. In 2013, he joined the Department of Electrical Engineering, Polytechnique Montreal, Montreal, QC, Canada, where he is currently an Associate Professor. His research interests include control systems, microgrid control, and smart grids.



Masoud Davari (S'08–M'17–SM'19) was born in Isfahan, Iran, on September 14, 1985. He received the B.Sc. degree in electrical engineering (power area) from the Isfahan University of Technology, Isfahan, in 2007, the M.Sc. degree in electrical engineering (power area) from the Amirkabir University of Technology (Tehran Polytechnic), Tehran, Iran, in 2010, and the Ph.D. degree in electrical engineering (energy systems area) from the University of Alberta, Edmonton, AB, Canada, in 2016. From January 2010 to December 2011, he was with Iran's

Grid Secure Operation Research Center and Iran's Electric Power Research Institute (EPRI), Tehran. From April 2015 to June 2017, he was a Senior R&D Specialist and Senior Consultant with Quanta-Technology Company, Markham, ON, Canada, in the field of the dynamic interaction of renewable energy systems with smart grids and control, protection, and automation of microgrids. In July 2017, he joined as a tenure-track Assistant Professor with the Allen E. Paulson College of Engineering and Computing, Department of Electrical and Computer Engineering, Georgia Southern University, Statesboro, GA, USA, where he was recommended and approved for being granted "'early" promotion to Associate Professor and award of "early" tenure on December 3, 2021. He is the Founder and the Director of the Laboratory for Advanced Power and Energy Systems (LAPES) in the state-of-the-art Center for Engineering and Research (CEaR) established in 2021 with Georgia Southern University. He has developed and implemented several experimental test rigs for research universities and the power and energy industry. He has also authored several papers published in IEEE Transactions and journals. His research interests include the dynamics, controls, and protections of different power electronic converters, which are utilized in the hybrid ac/dc smart grids, and hardware-in-the-loop (HIL) simulation-based testing of modernized power systems. Dr. Davari has been an Active Member and a Chapter Lead in the IEEE Power & Energy Society Task Force on "Innovative Teaching Methods for Modern Power and Energy Systems" since July 2020. He has been an Active Member and a Chapter Lead (for Chapter 3) in the IEEE Working Group P2004—a newly established IEEE working group entitled "Hardware-in-the-Loop (HIL) Simulation Based Testing of Electric Power Apparatus and Controls" for IEEE Standards Association since June 2017. He is an invited member of the Golden Key International Honour Society. He was the Chair of the Literature Review Subgroup of DC@Home Standards for the IEEE Standards Association from April 2014 to October 2015. He is an invited reviewer of several of the IEEE Transactions and journals, IET journals, Energies journal, and various IEEE conferences, the invited speaker at different universities and in diverse societies, and the Best Reviewer of the IEEE TRANSACTIONS ON POWER SYSTEMS in 2018 and 2020. He is the recipient of the 2019-2020 Allen E. Paulson College of Engineering and Computing (CEC) Faculty Award for Outstanding Scholarly Activity in the Allen E. Paulson CEC at Georgia Southern University and the Discovery and Innovation Award from the 2020-2021 University Awards of Excellence.



S. Milad Hoseinizadeh (S'22) received the B.Sc. and M.Sc. degrees in electrical engineering from Shahid Chamran University, Ahvaz, Iran, in 2011, and K. N. Toosi University of Technology, Tehran, Iran, 2013, respectively. He is currently working toward the PhD program in the Department of Electrical Engineering at Polytechnique Montreal, Montreal, Canada. His research interests include control systems, microgrid control, and smart grids.